A Potential Cathode for Quasi Solid-State Sodium-Ion Batteries with Trivalent Doping of La³⁺ in Sodium Iron Phosphate

P. Priyanka and B. Nalini[*],[iD]

Avinashilingam Institute for Home Science and Higher Education for Women, Coimbatore-641 043, India

*Corresponding author: E-mail: nalinicselvin11@gmail.com

In this work, a low cost and environmental friendly cathode material sodium iron phosphate ($NaFePO_4$) has been investigated with trivalent doping of lanthanum (La^{3+}). Maricite phase of $NaFePO_4$ exhibits 154 mAhg⁻¹ theoretical capacity and this phase is said to be electrochemically inactive, hence studies are focussed on enhancing the properties of $NaFePO_4$. Lanthanum exhibits a trivalent state and can be favourable on doping in the Fe site. Hence, an attempt is made to synthesize five different concentrations of La^{3+} in $NaFe_{1-x}La_xPO_4$ (x = 0.02, 0.04, 0.06, 0.08 and 0.1) of its first kind. An initial discharge capacity of 116 mAhg⁻¹ at a current density of 0.1 Ag⁻¹ has been achieved over 100 cycles when 0.02 concentration of La dopant in $NaFePO_4$ is constructed as cell with NaOH aqueous electrolyte. The La-doped $NaFePO_4$ at 0.02 concentration (NL2) exhibits higher specific capacity and cyclic stability. The initial discharge capacity of 36 mAh g⁻¹ at 0.5 A g⁻¹ was achieved over 500 cycles in the quasi-solid-state sodium battery analysis using a $CuS:Sn_2Sb_3$ anode and a PVA-NaOH electrolyte. This study shows a light on trivalent doping of La^{3+} with different concentrations and their effect as cathode when assembled as full cell for the first time.

Keywords: $NaFePO_4$, Trivalent doping, Lanthanum, Cathode, Quasi solid-state SIBs.

INTRODUCTION

Over the past two decades, lithium-ion batteries (LIBs) have majorly dominated the field of electrochemical energy storage devices. Still, difficulties such as high cost, thermal runaway, limitation on power density and inadequate lithium source are the barriers for expedient energy storage devices. The advancement of technology that makes use of alternative resources including sodium, magnesium, and potassium has been explored by researchers. Among all, a suitable alternate to lithium-ion batteries (LIBs) are found to be sodium-ion batteries (SIBs) [1,2] since sodium has gained focus due to the fact that sodium is abundant on earth's crust by 2.3% and India is the third country in producing sodium salts across the globe. It is more appropriate to focus and work on Na-ion batteries with a purview to bring up a technology that is devoid of any restricted atmosphere for assembly and should be capable of sufficing the demand of energy as well. Nevertheless, it is crucial to acknowledge that sodium-ion batteries encounter challenges such as reduced energy density in comparison to lithium-ion chemistries, along with restrictions in cycle life and rate capability.

Research and development efforts are ongoing to address these challenges and improve the performance of sodium-ion battery technology. One of the most important components of SIBs is the cathode material, which plays a vital role in determining the battery performance in terms of energy density, cycling stability and safety [3]. There are several types of cathode materials with its own advantages and disadvantages *viz.* $NaFePO_4$ [4], $NaMnPO_4$ [5], $NaCoO_2$ [6], $NaNiO_2$ [7], $Na_3V_2(PO_4)_3$ [8], $Na_2NiFe(CN)_6$ [9], *etc.* Among various cathode materials explored for SIBs, sodium iron phosphate ($NaFePO_4$) has reaped significant attention owing to its high theoretical capacity of 154 mAh g⁻¹, environmental friendliness and thermal stability [3,7]. There are two mineral forms of $NaFePO_4$ *i.e.* maricite and olivine. Maricite phase consists of sodium at octahedral sites and iron (Fe^{2+}/Fe^{3+}) at tetrahedral sites tuning up a three dimensional framework with high thermal stability [10] but is electrochemically inactive phase [11]. Hence, to improve the electrochemical activity of pure phase of $NaFePO_4$, researchers

focus towards enhancing the overall performance by either carbon incorporation/composites/surface modifications/doping strategies, *etc.*

The choice of dopant depends on the specific requirements of the battery such as desired capacity, cycling stability and voltage profile. Each dopant can have a different impact on the electrochemical properties of the material and extensive research is conducted to optimize the doping process for better battery performance. In the present work, La^{3+} has been chosen as a dopant in the synthesis of $NaFe_{1-x}La_xPO_4$ (x = 0.02, 0.04, 0.06, 0.08 and 0.1) using sol-gel method and this work explores the advantage of trivalent doping on the Fe site so as to enhance its electrochemical performance of pure $NaFePO_4$. Moreover, the impact of La doping on $NaFePO_4$, including improvements in specific capacity, cycling stability and rate capability, are discussed in this article and this kind of trivalent La^{3+} doping in $NaFePO_4$ is a maiden attempt. A higher value of charge capacity was obtained for La-0.02 composition sample with 116 mAh g^{-1} at 0.1 Ag^{-1}, 75% of the theoretical capacity over 100 cycles in aqueous three electrode half-cell system. The same sample when assembled as a full cell with the $NaFePO_4$: La as cathode *vs.* $CuS:Sn_2Sb_3$ anode and PVA-NaOH membrane as an electrolyte, the full cell could deliver 36 mAh g^{-1} as an initial capacity over 500 cycles at 0.1 A g^{-1}. In particular, sodium is not used as anode in the present case. A non-metallic full cell is also captive due to easy assembling and non-refinement of controlled atmosphere.

EXPERIMENTAL

Preparation of pure and La-doped $NaFePO_4$: Pure $NaFePO_4$ and La-doped $NaFePO_4$ were synthesized *via* sol-gel method. For the synthesis of pure $NaFePO_4$, appropriate amounts of ferrous oxalate dihydrate ($FeC_2O_4 \cdot 2H_2O$) and sodium nitrate were dissolved in 60 mL distilled water [Sol A]. Sol A was stirred until the salts get completely dissolved. A 10 mL of ammonium phosphate dihydrogen [Sol B] was stirred until it gets dissolved in water whereas citric acid (20 mL) [Sol C] was dissolved in distilled water under magnetic stirring. Sol B and C were added to Sol A and kept at 150 °C under magnetic

stirring until a gel was formed. The obtained gel was kept in water bath at 100 °C for 12 h for the removal of excess ammonia from the sample. The pure $NaFePO_4$ was finely ground and calcined at 700 °C for 2 h and named as NFP hereafter.

The same procedure was repeated for the La doping for different compositions *viz.* 0.02, 0.04, 0.06, 0.08 and 0.10 which are named as NL2, NL4, NL6, NL8 and NL10, respectively. Lanthanum nitrate hexahydrate ($LaNO_3 \cdot 6H_2O$) was used as a precursor taken along with sol A for all the samples.

Thermogravimetric analysis: In order to assess the possible reactions that can occur during NFP synthesis, the thermogravimetric profiles (Fig. 1a-b) of the NFP precursor sample was analyzed. This result was utilized to determine the appropriate calcination temperature for the synthesis of the desired product. The analysis was carried out from room temperature (RT) to 1000 °C in nitrogen atmosphere. The TGA curves can be divided into RT-100 °C, 100-173 °C, 173-265 °C, 265-339 °C, 339-483 °C, 483-746 °C and 746-1000 °C regions.

The first region shows 9.5% weight loss which is majorly from room temperature to 100 °C corresponding to the evaporation of moisture. The weight loss regions from 100-339 °C [12] corresponds to two processes of ferrous oxalate salt dehydration and decomposition. From the DTA curve, the peaks observed at 190, 265 and 332 °C were attributed to the ferrous oxalate decomposition. The next weight loss 339-483 °C may arise due to the decomposition of gelating agent *i.e.* citric acid. In other report, there is a prominent weight gain observed at 370 °C and 495 °C, which corresponds to the oxidation from Fe^{2+} to Fe^{3+} [13], which is not observed in present case. Hence there is no change of state/oxidation of iron. The temperature region from 480-700 °C shows a stable region of 8.14% residue after which the sample decomposes completely. The total weight loss of the precursor material is 63.56% as shown in Fig. 1a. From the DTA curve, an endothermic peak at 700 °C is observed and this temperature is chosen as the calcination temperature for the preparation of pure $NaFePO_4$ and the La-doped sample.

Material characterization: Thermal analysis was carried out using the instrument Thermal Analyzer (SDT Q600 V20.9). The X-ray diffraction analysis was carried out using the
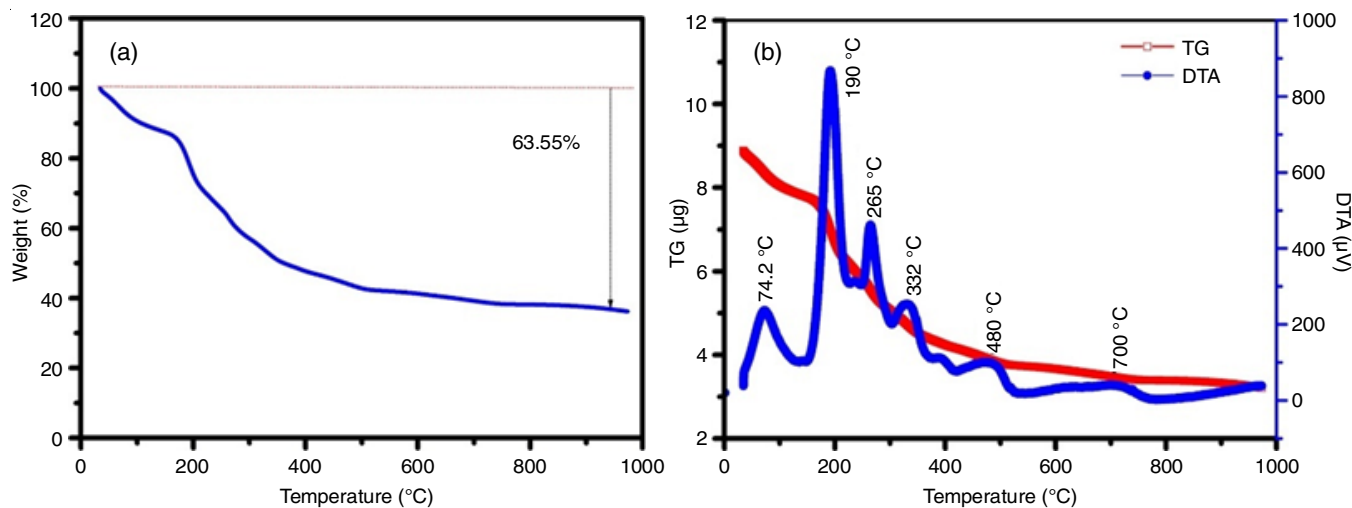
Fig. 1. Weight loss (a) and TG-DTA curves (b) of precursor NFP

PANalytical X'Pert Pro instrument with Cu$K\alpha$ radiation. The Raman analysis was done using excitation wavelength of 532 nm using HORIBA Labram instrument. The FESEM-EDX analysis was conducted using instrument Zeiss. Biologic SP-150 electrochemical workstation was used to analyze the cyclic voltammetry and electrochemical impedance analysis for the samples.

Electrochemical characterization

Three-electrode configuration: Using three-electrode system, the electrochemical studies were carried out for the pure and La-doped samples used as working electrodes which is composed of a mixture of active material and carbon black as conductive agent and polyvinylidene fluoride (PVDF) as binder in the ratio of 85:10:5. Then the mixture was mixed with N-methyl pyrrolidinone (NMP) solvent to form a slurry. Then the slurry was coated on an aluminium current collector and dried at 80 ºC to ensure the complete evaporation of NMP. The prepared electrode was tested in alkaline aqueous electrolyte *viz.* 1M NaOH dissolved in distilled water. The prepared electrode is tested using three electrode system. *i.e.* NFP, NL2, NL4, NL6, NL8 and NL10 as the working electrode, Ag/AgCl as reference electrode and platinum wire as the counter electrode.

Two-electrode configuration: The prepared pure NFP and La-doped NFP are subjected to full cell analysis to study the performance. The prepared samples were taken as cathode and $CuS:Sn_2Sb_3$ as an anode which has been already reported earlier [14] with PVA-NaOH gel polymer membrane. The prepared electrodes are cut into 2 cm × 2 cm as an active area and the PVA-NaOH membrane which was placed in between the two electrodes.

RESULTS AND DISCUSSION

X-ray diffraction (XRD): X-ray diffraction technique was used to determine the phase formation of the prepared pure and La-doped samples NL2, NL4, NL6, NL8 and NL10. Fig. 2 indicates the comparison of XRD patterns of NFP and the La-doped NFP samples. The diffraction peaks are observed
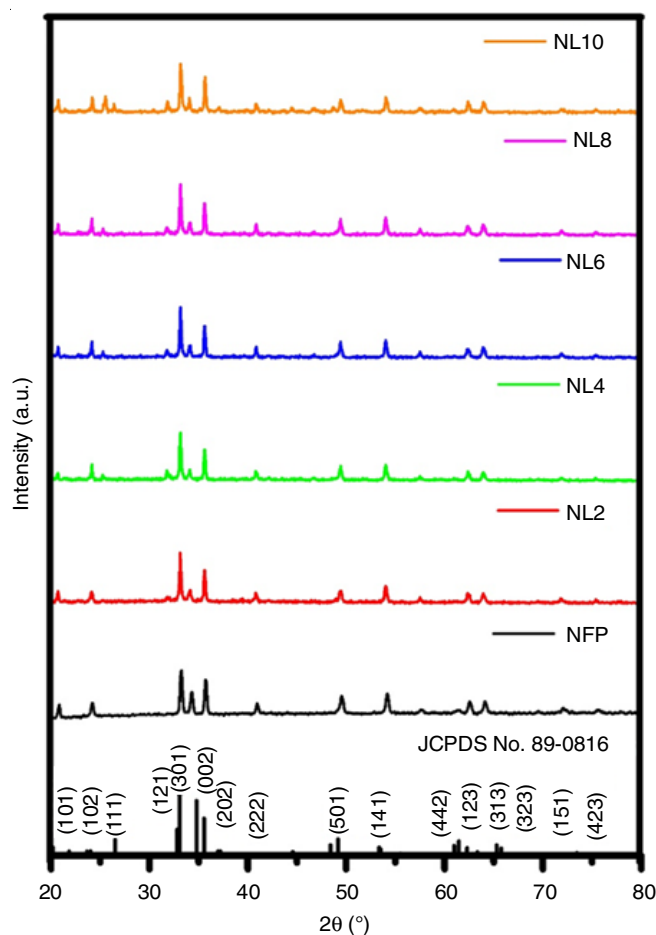
Fig. 2. XRD pattern of NFP and La-doped NFP

at 2θ = 20.8º, 24.13º, 33.14º, 34.26º, 35.71º, 40.99º, 49.59º, 54.10º, 57.60º, 62.63º, 64.17º, 69.63º, 672.20º, 75.68º corresponding to the *hkl* planes of (101), (111), (220), (400), (121), (202), (511), (322), (013), (303), (621), (323), (042) and (801), respectively. All the prominent diffraction peaks are well-indexed to ordered orthorhombic structure with a space group of *Pnma* [15], which matches well with the JCPDS Card No. 89-0816.
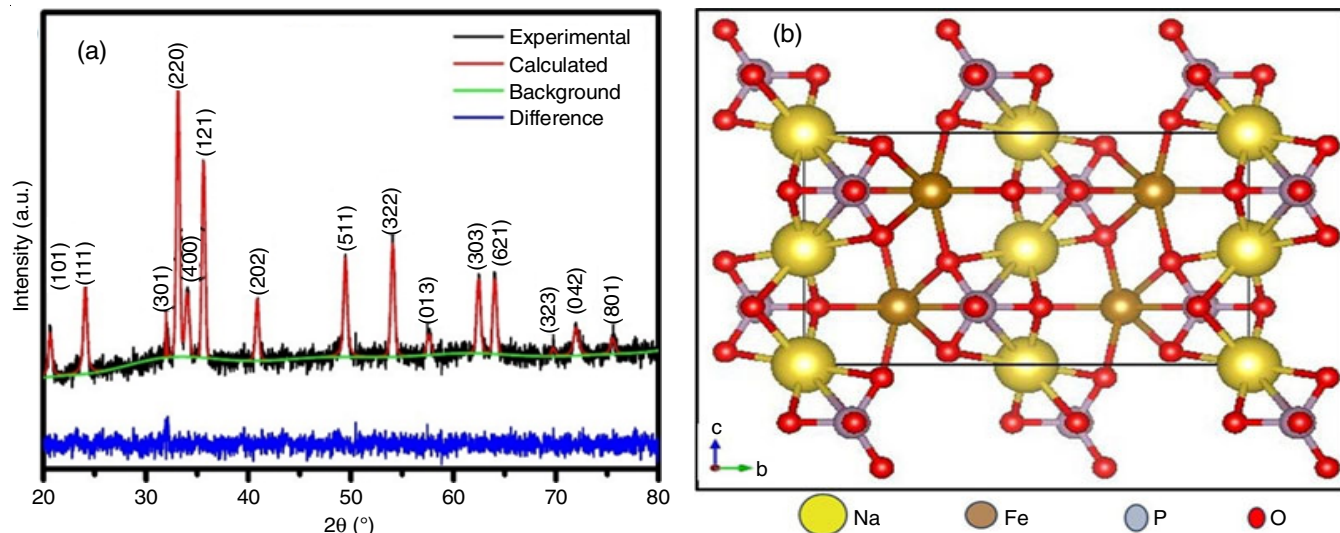
Fig. 3. (a) Rietveld refinement of NFP and (b) atomic arrangement of NFP drawn using VESTA software

Fig. 3a shows the Rietveld refined XRD pattern of pure NFP and the parameters of fit are R_{wp} = 2.317% and GOF = 1.80, which represents a good fit and the corresponding structure drawn from VESTA software is shown in Fig. 3b. For other samples NL2, NL4, NL6, NL8 and NL10, the peaks observed were indexed to orthorhombic structure of $NaFePO_4$. All the peaks are very sharp, which shows the high crystallinity of the prepared samples. The ionic radii of dopant La^{3+} is 1.06 Å. On doping with La at lower concentrations, there are no remarkable changes observed in the lattice parameters. When doping concentration exceeds above 0.04, lattice parameters tend to increase. The volume of the unit cell increases from 273.45 to 298.96 Å^3 on doping from 0.02 to 0.1 concentrations of La. The average crystallite size, calculated by Debye Scherrer's equation, were 34.9, 15.21, 56.3, 61.2, 65.9 and 78.9 nm for pure NFP, NL2, NL4, NL6, NL8 and NL10 samples, respectively. The crystallite size decreased for the NL2 sample as 15.21 nm and increases above the 0.04 concentration. The addition of La^{3+} dopant with the experimental evidences are matched from the XRD analysis where a theoretical study on yet another composition reports the evidences of La^{3+} doping [16].

Raman analysis: The structure of pure $NaFePO_4$ and all the La-doped $NaFePO_4$ were investigated by laser Raman spectroscopy. Fig. 4 shows the Raman spectra of $NaFePO_4$, the peaks at 221, 291, 403, 606 and 1308 cm^{-1} are observed. In pure NFP, the peaks corresponding to Fe-O vibrations are observed at 221, 291, 486 cm^{-1} [11,15]. The major peak corresponding to PO_4^{3-} deformation of $NaFePO_4$ phase is present at 403 cm^{-1} and has been shifted towards higher wavenumbers *viz.*, 406, 409, 406, 506 and 520 cm^{-1} of NL2, NL4, NL6, NL8 and NLP1, respectively. The higher wavenumber shift observed in the La-doped samples may be due to the lattice strain caused while doping [17,18]. The distinct peak at 1338-1308 cm^{-1}
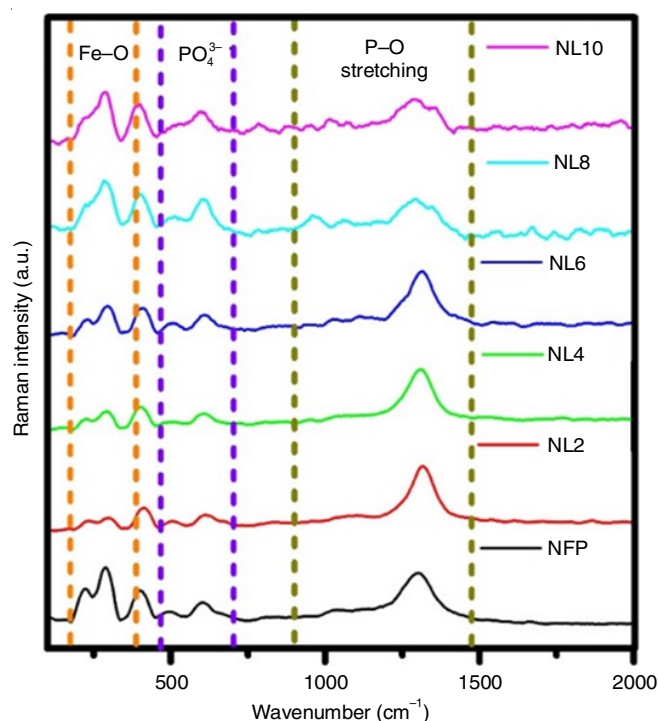
Fig. 4. Raman spectra of NFP and La-doped NFP

corresponds to P=O stretching vibration in all the samples indicating that the doped samples are also having stability due to this unaltered PO_4 framework [19].

FESEM analysis: The morphological analysis is studied using FESEM technique where the pure NFP exhibits a stacked plate like morphology (Fig. 5a). The doped samples of concentration 0.02 (Fig. 5b) and 0.04 (Fig. 5c) shows a preserved nanoplates formation which further vanishes at higher doping concentrations of La *viz.* NL6 (Fig. 5d), NL8 (Fig. 5e) and NL10
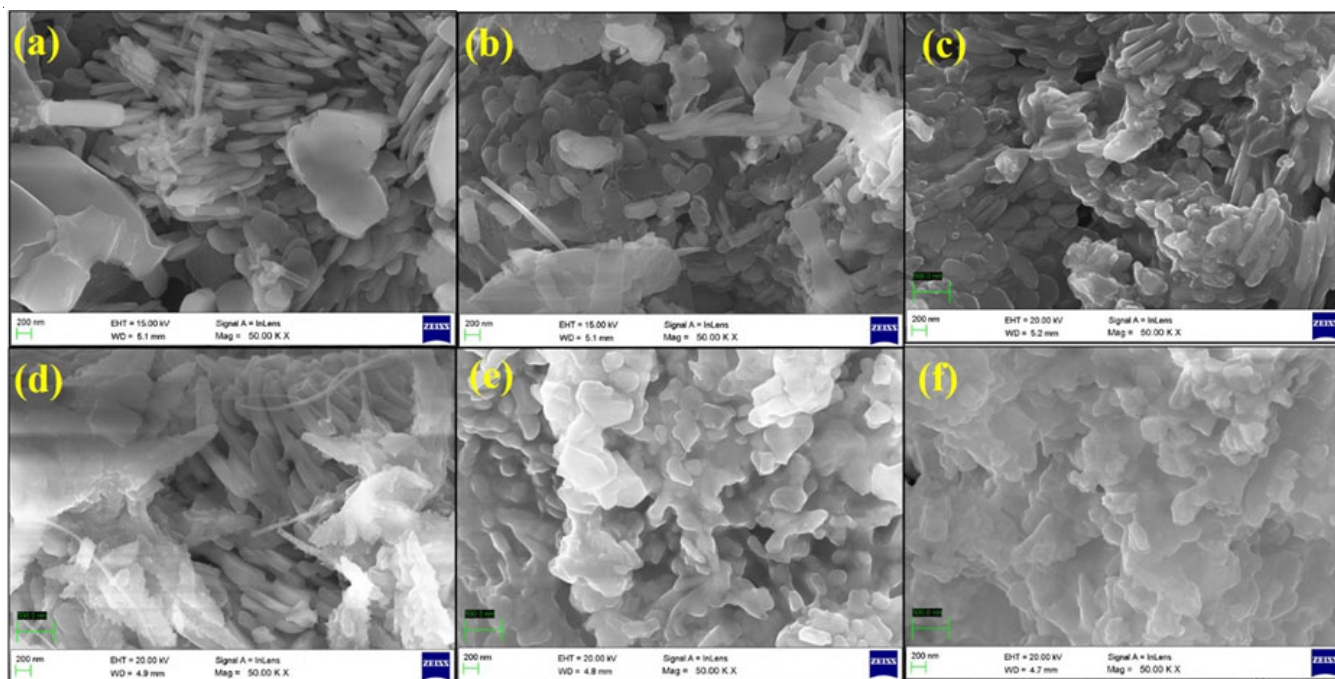
Fig. 5. FESEM micrographs of (a) NFP, (b) NL2, (c) NL4, (d) NL6, (e) NL8 and (f) NL10

(Fig. 5f). Severe agglomeration of particles were also observed which shows that particle growth upon doping with higher concentrations which also was observed in XRD analysis as increased crystallite size.

The existence of the elements Na, Fe, P and O were confirmed in pure NFP sample, through the elemental results of EDAX for all the pure and doped samples as shown in Fig. 6a-f. Whereas in the case of NL2, NL4, NL6, NL8 and NL10 compositions, the atomic weight ratio varies from one another as shown in the inset of the EDX spectrum. The concentration of La varies for all the compositions indicating the degree of doping. The existence of oxygen was observed at the varied levels in all the samples, which confirmed that the element La is present and doped into NFP in all the varied compositions. Since no formation of oxide was detected by Raman or XRD analyses, thus it is concluded that the presence of oxygen was due to the electron microscope chamber's low vacuum.

XPS analysis: The surficial analysis was carried out using X-ray photoelectron spectroscopy for NFP pure (Fig. 7a-e) and NL2 (Fig. 8a-e) samples for comparison. Fig. 7a shows the survey spectrum of NFP confirming the presence of Na, Fe, P, O elements of pure NFP. The presence of Na is confirmed by the characteristic peak present at 1070.46 eV for both NFP and NL2 samples (Fig. 7a and Fig. 8a) and the spectrum of Fe2p is shown in Fig. 7d, which is unraveled into two peaks at 723.78 eV and 710.12 eV corresponding to the Fe2p$_{1/2}$ and Fe2p$_{3/2}$ [10] state of Fe^{2+}. The same deconvolution of Fe peaks are present in NL2 sample. The presence of P2p can be seen

from Fig. 7e at 132.38 eV, which is also present in NL2 sample (Fig. 8e) at the same point. In NL2 sample, the presence of La at 835.18 eV (Fig. 8f) is confirmed whereas pure NFP does not show this peak. The XPS results showed that La dopant was successfully integrated into pure NFP without altering structural stability as observed in the XRD results.

Electrochemical characterization

Three-electrode aqueous system: To investigate the redox processes that take place at the electrode surface during reaction with the electrolyte, cyclic voltammetry (CV) analysis was performed. The cathodic component of SIBs play a vital role in intercalation/de-intercalation of sodium ions back and forth to achieve a reversible process. Fig. 9a shows the comparison of CV curves of pure NFP, NL2, NL4, NL6, NL8 and NL10. The pure NFP shows only a prominent oxidation peak whereas reduction peak has not been observed. According to the literature, pure NFP of maricite phase is considered to be electrochemically inactive [11], which means that it does not exhibit significant redox processes. Among the doped samples, NL2 exhibits a prominent redox peak with higher current values, *i.e.* two oxidative peaks and one reduction peak. Usually two oxidative peaks represent the intercalation of two species which may correspond to the intermediaries of NaFePO$_4$ [20]. Eventually in NL8 and NL10, the activity of the electrodes is too low with a reduced current values. The redox process was observed only till NL6 whereas in, NL8 and NL10 shows no redox activity indicating the dopant completely inhibits the electrochemical activity.
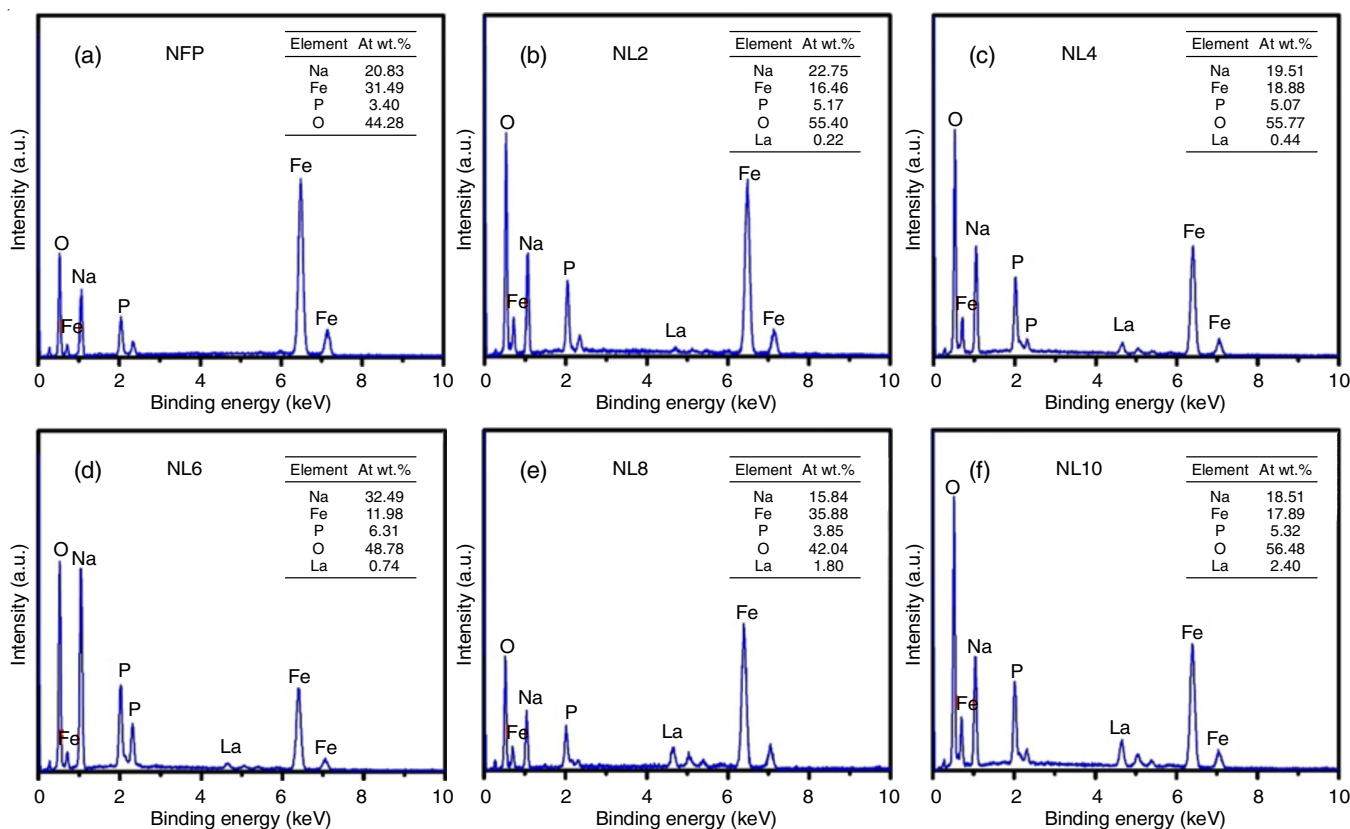
Fig. 6. EDX spectrum of (a) NFP, (b) NL2, (c) NL4, (d) NL6, (e) NL8 and (f) NL10
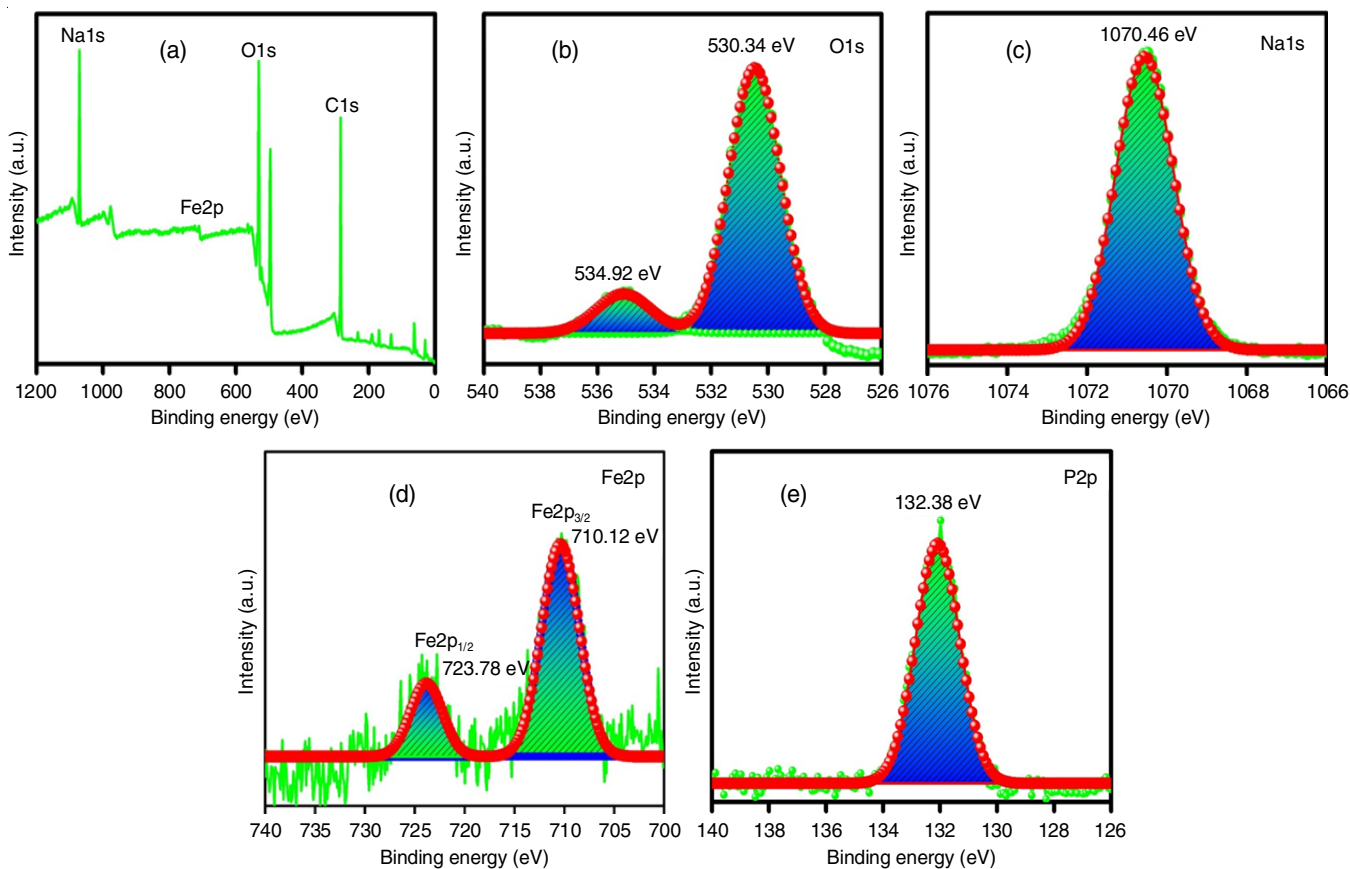
Fig. 7. XPS spectrum of NFP pure (a) survey scan, (b) O1s, (c) Na1s, (d) Fe2p and (e) P2p
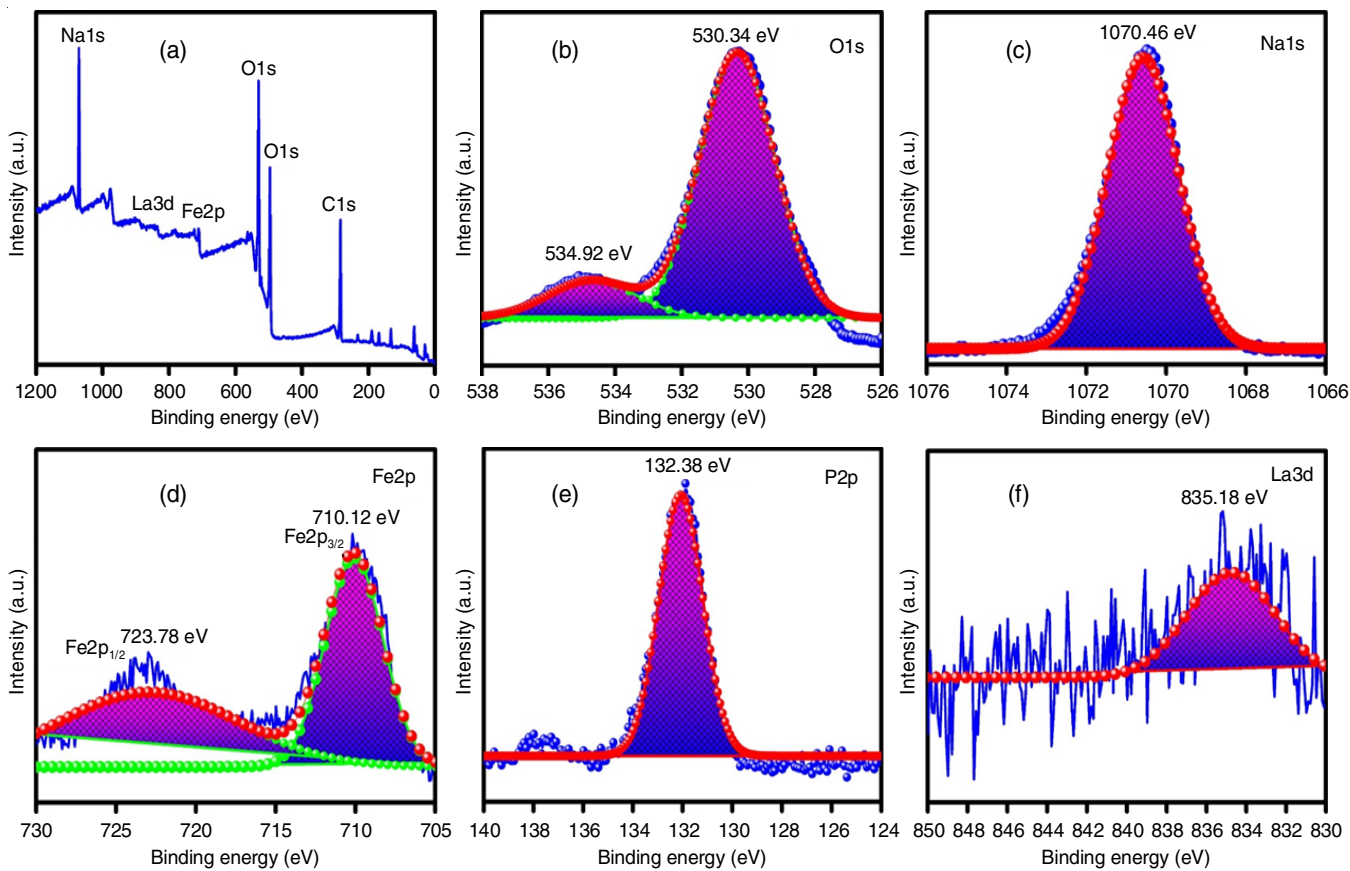
Fig. 8. XPS spectrum of NL2 (a) survey scan, (b) O1s, (c) Na1s, (d) Fe2p, (e) P2p and (f) La3d
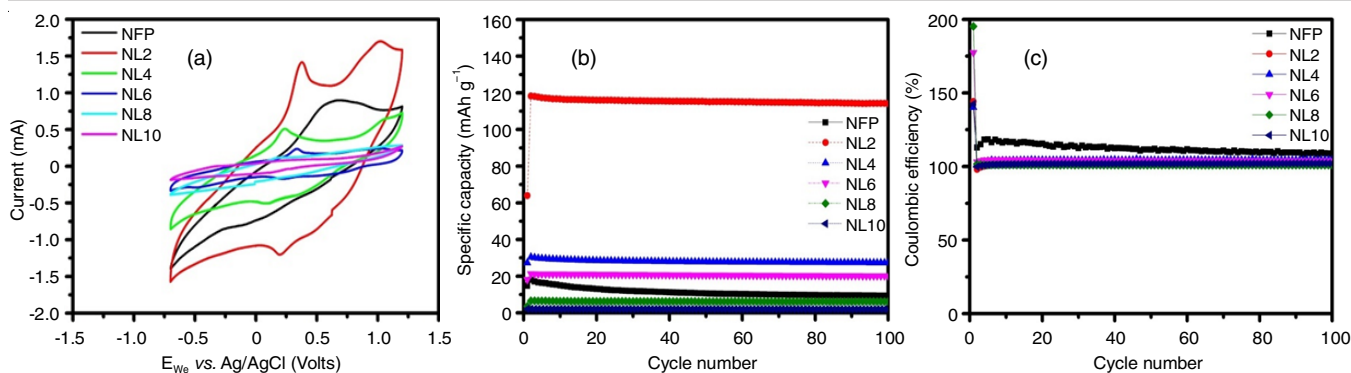
Fig. 9. (a) CV curves of NFP, NL2, NL4, NL6, NL8, NL10, (b) Comparison of specific charge capacity of NFP, NL2, NL4, NL6, NL8, NL10 and (c) Coulombic efficiency comparison of NFP, NL2, NL4, NL6, NL8, NL10

The galvanostatic charge-discharge (GCD) analysis was recorded for the all the samples and the specific capacity observed for the NFP, NL2, NL4, NL6, NL8, NL10 samples at 0.1 Ag⁻¹ are shown in Fig. 9b. A stable capacity of 20 mAh g⁻¹ was achieved for pure NFP. NL2 shows an initial capacity of 64 mAh g⁻¹, which increases and maintains stability at 116 mAh g⁻¹ over 100 cycles. NL4 shows a specific capacity of 32 mAh g⁻¹ and NL6 shows much reduced value of specific capacity of 21.5 mAh g⁻¹ over 100 number of cycles. In case of NL8 and NL10, the specific capacity values fall below 10 mAh g⁻¹ indicating less performance of the electrodes as expected from the structural studies of XRD and Raman. The coulombic efficiency of the pure and La doped samples are shown in Fig. 9c. The NFP pure indicates a value more that 100% indicating some side reactions happening during the cycling process. And all the La-doped samples shows a value nearing to 100% indicating good stability of the electrodes. Although less capacity values were observed for NL4, NL6, NL8, NL10 than NL2,

the capacity remains stable when cycling and coulombic efficiency also remains nearly 100% for all the cases. A higher capacity of 116 mAh g⁻¹ is obtained for NL2, which may be due to higher wettability achieved by reduced crystallite size, no agglomeration of particles and optimal occupancy of La in unit cells of NFP.

Table-1 shows the reported the literatures on sodium iron phosphate based cathodes along with their electrochemical performances. The capacity obtained are not compared directly with the available literature since the present system is aqueous with NaOH based electrolyte and all the other literatures mentioned are done with non-aqueous electrolyte. For further inference, the electrochemical impedance analysis was conducted before and after cycling (Fig. 10a-g). The internal resistance of all the samples before and after cycling are very low indicating good reversibility of the electrodes over cycling. In sample NL2, the overall resistance values before and after cycling does not show much difference and remains comparatively lower than

TABLE-1
ELECTROCHEMICAL PERFORMANCE OF REPORTED LITERATURES BASED ON NaFePO₄

Material used	Method of preparation	Electrochemical performance	Ref.
Amorphous NaFePO₄	Simulated melt-quenching	Capacity of 142 mAh g⁻¹ with 95% capacity retention over 200 cycles.	[20]
Sodium iron phosphate (NFP)	Chemical delithiation/sodiation method	Excellent cycling performance with a capacity of 85 mAh g⁻¹ and a capacity retention of 95% over 100 cycles	[21]
Carbon-coated Na₂FeP₂O₇	Facile urea-nitrate combustion method	Stable reversible capacity of 78 mAh g⁻¹ at 1 C for 300 cycles and retains a reversible capacity of 18 mAh g⁻¹ for 20 cycles even at a current density reaching up to 50 C.	[22]
Carbon-coated NaFePO₄ (NaFePO₄/C)	Two-step solid state method	Initial reversible capacity of 48.8 mAh g⁻¹ at 0.05 C rate over 100 cycles.	[23]
Maricite NaFePO₄ powder	Solid-state reaction method	Capacity of 142 mAh g⁻¹ (92% of the theoretical value) at the first cycle.	[10]
Na/NaFePO₄ with an olivine crystal structure	Electrochemical sodiation method	A maximum discharge capacity of NaFePO₄ was 120 mAh g⁻¹ at 0.05C rate	[24]
Carbon-coated olivine NaFePO₄ (C-NaFePO₄)	Chemical delithiation and subsequent electrochemical sodiation method	A reversible capacity of 100 mAh g⁻¹ at 0.1C rate	[25]
NaFePO₄	Hydrothermal route	A discharge capacity of 147 mAh g⁻¹	[26]
NaFePO₄/NaFePO₄F	Solid state method	Charge-discharge capacity of NaFePO₄ is 19 mAh g⁻¹ and carbon coated NaFePO₄F shows discharge capacity of 116 mAh g⁻¹ at 0.1C rate	[27]
NaFePO₄/NaFe₀.₁₈La₀.₀₂PO₄	Sol-gel method	Capacity of 20 mAh g⁻¹ at 0.1 Ag⁻¹ is achieved for pure sample and 116 mAh g⁻¹ for 0.02 La doped NaFePO₄ at 0.1 Ag⁻¹ over 100 cycles	Present work
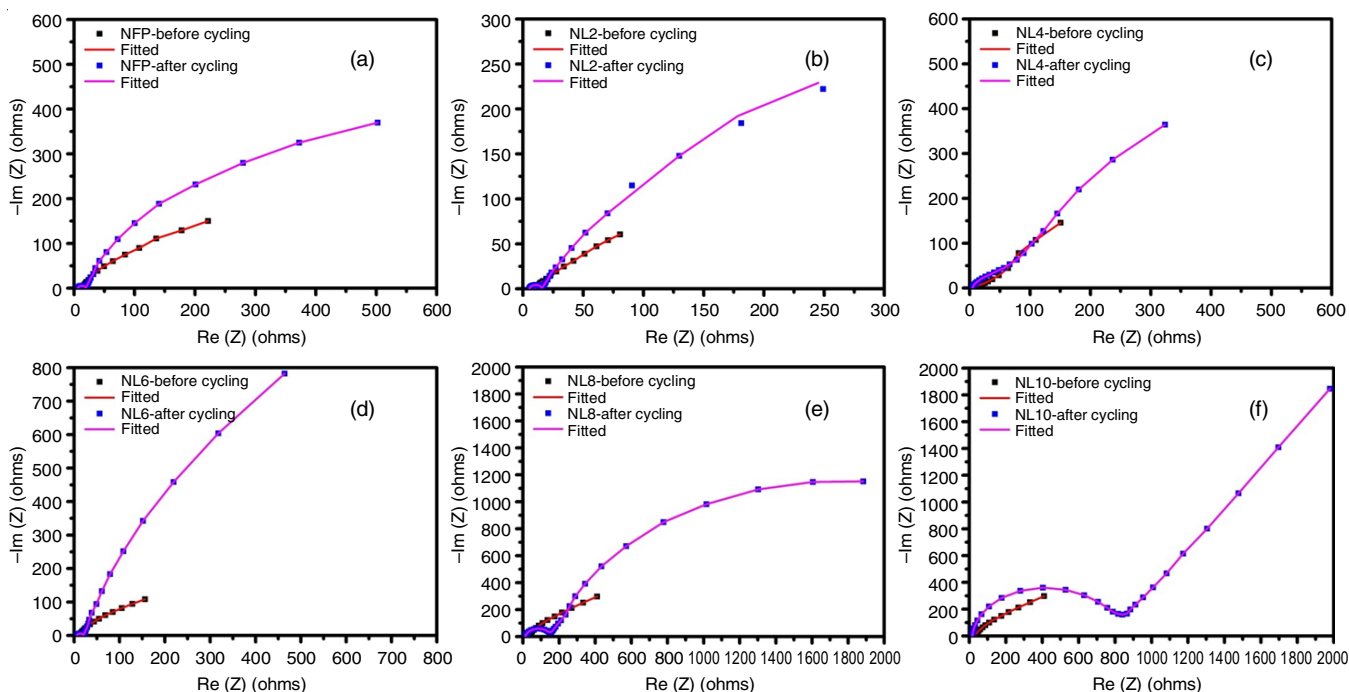
Fig. 10. EIS graphs S (a) NFP, (b) NL2, (c) NL4, (d) NL6, (e) NL8 and (f) NL10

pure NFP indicating better reversible kinetics at the electrodes (Table-2). On increasing the concentration from samples NL4 to NL10, the resistance values also increased.

Two-electrode device analysis

CV analysis: The devices NFP/PVA-NaOH/CuS-Sn$_2$Sb$_3$ and NL2/PVA-NaOH/CuS-Sn$_2$Sb$_3$ were constructed and subjected to cyclic voltametric analysis and the comparison of both full cells (Fig. 11a). The pure NFP shows a potential window from 0.2 V to 2.2 V and the potential window extends from 0.5 V to 2.2 V for the NL2 sample as observed from the CV curves. A single redox process with oxidation and reduction peaks at 1.60 V and 0.32 V was observed for pure NFP whereas in NL2, 1.50 V and 1.86 V were the two oxidation peaks observed with a reduction peak at 0.69 V. Two oxidation peaks were observed with NL2, which may correspond to the reactions happening. The full cell assembled with pure NFP and NL2 shows different kinetics.

Galvanostatic charge-discharge (GCD) analysis: From the GCD analysis, the specific capacity and capacity retention has been evaluated. The full cell with NFP pure shows a stable capacity of 19.5 mAh g^{-1} and it maintains stable over 500 number of cycles with 70% of coulombic efficiency and a capacity retention of 100% (Fig. 11c). When assembled with NL2 as cathode in the full cell (Fig. 11d), 36 mAh g^{-1} of initial capacity is found and 40% fade is observed over 200 cycles with a stable coulombic efficiency of 90%. A higher value of capacity is achieved for the full cell assembled with NL2. The charge-discharge curves of full cell with NL2 is shown in Fig. 11b and the impedance of full cell assembled with NFP shows an increased cell resistance after cycling than NL2 shown in Fig. 11e. The electrochemical performance of full device assembled with NL2 shows good performance however the pure NFP shows a higher stability thus indicating that the trivalent doping of La^{3+} has individually shown good performance but when assembled as full cells shows two oxidation peaks and a higher initial

TABLE-2 EIS PARAMETERS BEFORE AND AFTER CYCLING FOR NFP, NL2, NL4, NL6, NL8 AND NL10								
Fitted parameters		R1 (Ω)	R2 (Ω)	R3 (Ω)	Q1 (× 10⁻⁶)	a₁	Q2 (× 10⁻³)	a₂
NFP	Before	5.66	11.25	110.24	85.58	0.84	3.47	0.78
	After	6.61	20.26	510.93	48.90	0.65	54.91	0.91
NL2	Before	5.28	9.75	79.85	74.62	0.81	2.541	0.65
	After	5.32	16.12	280.98	38.42	0.799	4.949	0.92
NL4	Before	1.37	18.92	150.80	88.49	0.88	7.93	0.72
	After	4.80	14.20	323.09	42.98	0.72	23.84	0.58
NL6	Before	5.85	11.09	165.98	98.46	0.89	5.041	0.62
	After	6.40	29.96	650.92	56.98	0.818	73.831	0.98
NL8	Before	13.03	22.89	510.98	98.40	0.88	58.58	0.53
	After	18.98	157.15	2051.08	39.45	0.92	85.98	0.65
NL10	Before	13.50	23.53	424.06	89.50	0.89	49.58	0.55
	After	16.12	832.75	2859.03	28.94	0.94	94.89	0.64
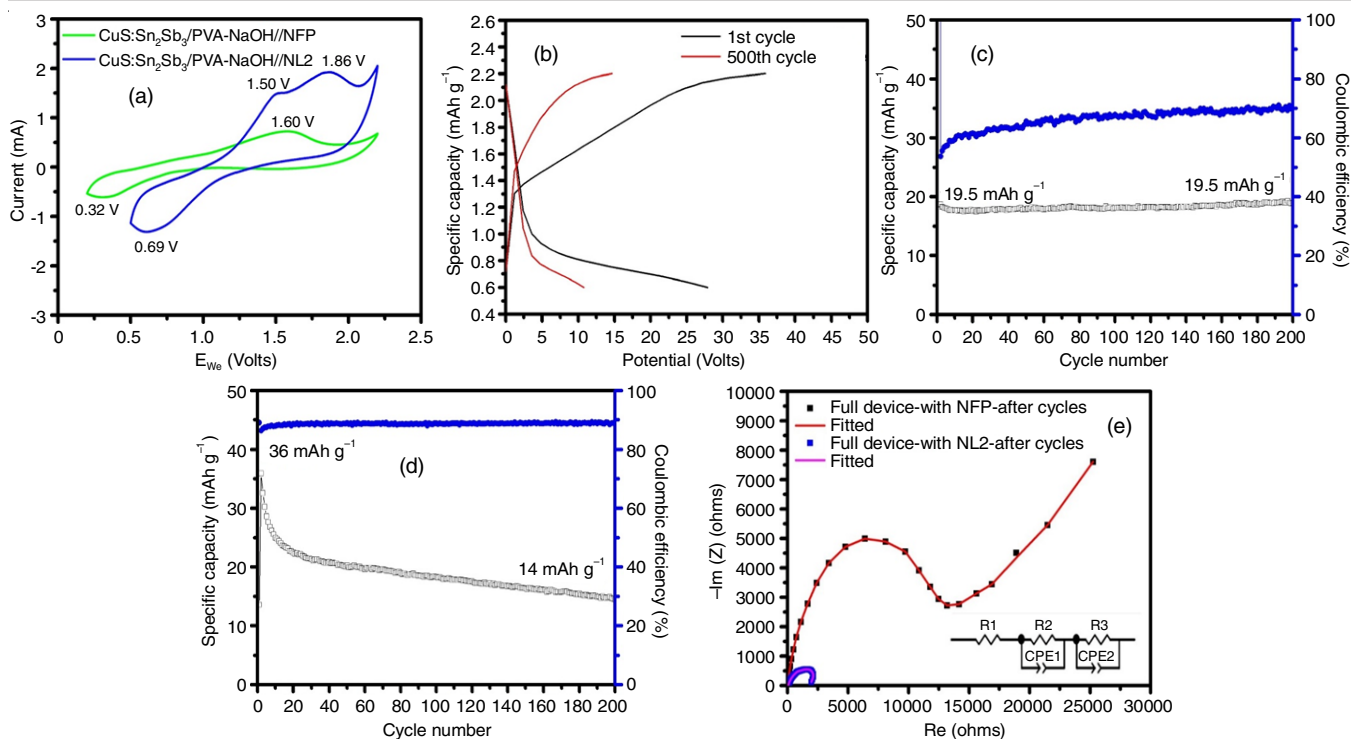
Fig. 11. (a) Comparison of CV curves of full cell assembled with NFP and NL2 as cathode, (b) GCD curve of full cell with NL2 cathode, cyclic stability of (c) NFP as cathode (d) NL2 as cathode at 0.5 Ag⁻¹ (e) comparison of impedance after cycles for NFP and NL2 as cathode in the full cell

discharge capacity value of 36 mAh g⁻¹ but decays over cycling, which may be due to non-compatibility with the selected anode.

Conclusion

A first attempt on doping a trivalent element La³⁺ on Fe site of maricite NaFePO₄ was studied. A higher capacity of 116 mAh g⁻¹ has been achieved for 0.02 concentration of (NL2) La doped in NaFePO₄ sample. The nanoplates like morphology has been preserved till 0.06 concentration of La doping in the host and severe agglomeration of particles was observed when dopant concentration increased. The cathode NL2 demonstrates the highest level of performance when used as a full cell alongside the anode CuS:Sn₂Sb₃ and the PVA-NaOH electrolyte. Many reports show full cell assembled with organic based electrolytes, but the full cell was not of quasi-solid state battery type. Therefore, an initial experiment was conducted using the produced anode and PVA-NaOH membrane electrolyte. The sample NL2 exhibited an initial capacity of 36 mAh g⁻¹ at a rate of 0.1 A g⁻¹ across a span of 500 cycles. The results obtained shows that La as a potential dopant but on comparison of performance with the full cell, 60% retention was observed which might be due to interfacial reactions that can be improved further. However, this result stands high in its place of quasi solid-state sodium-ion batteries.

CONFLICT OF INTEREST

The authors declare that there is no conflict of interests regarding the publication of this article.

REFERENCES

1. A. Manthiram, *ACS Cent. Sci.*, **3**, 1063 (2017);
    https://doi.org/10.1021/acscentsci.7b00288
2. J.Y. Hwang, S.T. Myung and Y.K. Sun, *Chem. Soc. Rev.*, **46**, 3529 (2017);
    https://doi.org/10.1039/C6CS00776G
3. P. Gupta, S. Pushpakanth, M.A. Haider and S. Basu, *ACS Omega*, **7**, 5605 (2022);
    https://doi.org/10.1021/acsomega.1c05794
4. S. Altundag, S. Altin, S. Yasar and E. Altin, *Vacuum*, **210**, 111853 (2023);
    https://doi.org/10.1016/j.vacuum.2023.111853
5. V. Priyanka, G. Savithiri, R. Subadevi and M. Sivakumar, *Appl. Nanosci.*, **10**, 3945 (2020);
    https://doi.org/10.1007/s13204-020-01506-8
6. B.V. Rami Reddy, R. Ravikumar, C. Nithya and S. Gopukumar, *J. Mater. Chem. A Mater. Energy Sustain.*, **3**, 18059 (2015);
    https://doi.org/10.1039/C5TA03173G
7. L. Wang, J. Wang, X. Zhang, Y. Ren, P. Zuo, G. Yin and J. Wang, *Nano Energy*, **34**, 215 (2017);
    https://doi.org/10.1016/j.nanoen.2017.02.046
8. Y. Zhu, H. Xu, J. Ma, P. Chen and Y. Chen, *J. Solid State Chem.*, **317**, 123669 (2023);
    https://doi.org/10.1016/j.jssc.2022.123669
9. X.H. Ma, Y.Y. Wei, Y.D. Wu, J. Wang, W. Jia, J.H. Zhou, Z.F. Zi and J.M. Dai, *Electrochim. Acta*, **297**, 392 (2019);
    https://doi.org/10.1016/j.electacta.2018.11.063
10. J. Kim, D.H. Seo, H. Kim, I. Park, J.K. Yoo, S.K. Jung, Y.U. Park, W.A. Goddard III and K. Kang, *Energy Environ. Sci.*, **8**, 540 (2015);
    https://doi.org/10.1039/C4EE03215B

11. D. Wang, Y. Wu, J. Lv, R. Wang and S. Xu, *Colloids Surf. A Physicochem. Eng. Asp.*, **583**, 123957 (2019); https://doi.org/10.1016/j.colsurfa.2019.123957

12. P. Hermankova, M. Hermanek and R. Zboril, *Eur. J. Inorg. Chem.*, **2010**, 1110 (2010); https://doi.org/10.1002/ejic.200900835

13. M. Hiratsuka, T. Honma and T. Komatsu, *J. Alloys Compd.*, **885**, 160928 (2021); https://doi.org/10.1016/j.jallcom.2021.160928

14. P. Priyanka, B. Nalini, G.G. Soundarya, P. Christopher Selvin and D.P. Dutta, *Front. Energy Res.*, **11**, 1266653 (2023); https://doi.org/10.3389/fenrg.2023.1266653

15. F. Xiong, Q. An, L. Xia, Y. Zhao, L. Mai, H. Tao and Y. Yue, *Nano Energy*, **57**, 608 (2019); https://doi.org/10.1016/j.nanoen.2018.12.087

16. N. Kuganathan and A. Chroneos, *Materials*, **12**, 1348 (2019); https://doi.org/10.3390/ma12081348

17. Y. Fang, J. Qian, X. Ai, H. Yang and Y. Cao, *Nano Lett.*, **14**, 339 (2014); https://doi.org/10.1021/nl501152f

18. X. Ma, J. Xia, X. Wu, Z. Pan and P.K. Shen, *Carbon*, **146**, 78 (2019); https://doi.org/10.1016/j.carbon.2019.02.004

19. D. Tibebe, Y. Kassa and A.N. Bhaskarwar, *BMC Chem.*, **13**, 107 (2019); https://doi.org/10.1186/s13065-019-0628-1

20. J.H. Bong and S. Adams, *Funct. Mater. Lett.*, **14**, 2141006 (2021); https://doi.org/10.1142/S179360472141006X

21. M. Hilder, P.C. Howlett, D. Saurel, H. Anne, M. Casas-Cabanas, M. Armand, T. Rojo, D.R. MacFarlane and M. Forsyth, *J. Power Sources*, **406**, 70 (2018); https://doi.org/10.1016/j.jpowsour.2018.09.102

22. X. Chen, K. Du, Y. Lai, G. Shang, H. Li, Z. Xiao, Y. Chen, J. Li and Z. Zhang, *J. Power Sources*, **357**, 164 (2017); https://doi.org/10.1016/j.jpowsour.2017.04.075

23. L. Zhao, D. Zhou, W. Huang, X. Kang, Q. Shi, Z. Deng, X. Yan and Y. Yu, *Int. J. Electrochem. Sci.*, **12**, 3153 (2017); https://doi.org/10.20964/2017.04.35

24. N. Wongittharom, T.C. Lee, C.H. Wang, Y.C. Wang and J.K. Chang, *J. Mater. Chem. A Mater. Energy Sustain.*, **2**, 5655 (2014); https://doi.org/10.1039/c3ta15273a

25. Y. Zhu, Y. Xu, Y. Liu, C. Luo and C. Wang, *Nanoscale*, **5**, 780 (2013); https://doi.org/10.1039/C2NR32758A

26. K. Zaghib, J. Trottier, P. Hovington, F. Brochu, A. Guerfi, A. Mauger and C.M. Julien, *J. Power Sources*, **196**, 9612 (2011); https://doi.org/10.1016/j.jpowsour.2011.06.061

27. N.V. Kosova, V.R. Podugolnikov, E.T. Devyatkina and A.B. Slobodyuk, *Mater. Res. Bull.*, **60**, 849 (2014); https://doi.org/10.1016/j.materresbull.2014.09.081